Editors' Suggestion

From spin liquid to magnetic ordering in the anisotropic kagome Y-kapellasite $Y_3Cu_9(OH)_{19}Cl_8$: A single-crystal study

Dipranjan Chatterjee,[1] Pascal Puphal,[2] Quentin Barthélemy,[1] Jannis Willwater,[3] Stefan Süllow,[3] Christopher Baines,[4] Sylvain Petit,[5] Eric Ressouche,[6] Jacques Ollivier,[7] Katharina M. Zoch,[8] Cornelius Krellner,[8] Michael Parzer,[9] Alexander Riss,[9] Fabian Garmroudi,[9] Andrej Pustogow,[9] Philippe Mendels,[1] Edwin Kermarrec,[1] and Fabrice Bert[1]

[1]*Université Paris-Saclay, CNRS, Laboratoire de Physique des Solides, 91405, Orsay, France*
[2]*Max-Planck-Institute for Solid State Research, Heisenbergstraße 1, 70569 Stuttgart, Germany*
[3]*Institut für Physik der Kondensierten Materie, Technische Universität Braunschweig, 38106 Braunschweig, Germany*
[4]*Laboratory for Muon-Spin Spectroscopy, Paul Scherrer Institut, 5232 Villigen, Switzerland*
[5]*LLB, CEA, CNRS, Université Paris-Saclay, CEA Saclay, 91191 Gif-sur-Yvette, France*
[6]*Université Grenoble Alpes, CEA, IRIG, MEM, MDN, 38000 Grenoble, France*
[7]*Institut Laue-Langevin, 38042 Grenoble, France*
[8]*Physikalisches Institut, Goethe-Universität Frankfurt, Frankfurt am Main 60438, Germany*
[9]*Institute of Solid State Physics, TU Wien, 1040 Vienna, Austria*

(Received 25 November 2022; revised 22 February 2023; accepted 13 March 2023; published 28 March 2023)

$Y_3Cu_9(OH)_{19}Cl_8$ realizes an original anisotropic kagome model hosting a rich magnetic phase diagram [Hering *et al.*, npj Comput. Mater. **8**, 10 (2022)]. We present an improved synthesis of large phase-pure single crystals via an external gradient method. These crystals were investigated in detail by susceptibility, specific heat, thermal expansion, neutron scattering, and local μSR and NMR techniques. At variance with polycrystalline samples, the study of single crystals gives evidence for subtle structural instabilities at 33 and 13 K which preserve the global symmetry of the system and thus the magnetic model. At 2.1 K the compound shows a magnetic transition to a coplanar (1/3,1/3) long-range order as predicted theoretically. However, our analysis of the spin-wave excitations yields magnetic interactions which locate the compound closer to the phase boundary to a classical *jammed* spin-liquid phase. Enhanced quantum fluctuations at this boundary may be responsible for the strongly reduced ordered moment of the Cu^{2+}.

DOI: 10.1103/PhysRevB.107.125156

I. INTRODUCTION

Low-dimensional materials with strong magnetic frustration, such as compounds with decoupled antiferromagnetic kagome layers, are prototypical systems to search for an experimental realization of the quantum spin-liquid (QSL) state [1,2]. This long sought state features no static magnetic order, despite sizable magnetic interactions, but rather macroscopic entanglement and fractional excitations. Experimental signatures of a QSL state in kagome materials were found first in herbertsmithite, $ZnCu_3(OH)_6Cl_2$ [3,4], and in the closely related Zn-doped barlowite [5,6]. Thus Cu-based systems with a perfect kagome layer have been strongly investigated.

Around the $A^{2+}Cu_3(OH)_6Cl_2$ family [7] a new similar series of compounds has been found with $A^{3+}Cu_3(OH)_6Cl_3$ [7–9], which realizes perfect kagome layers in a kapellasite-type structure. However, for Y^{3+} the compound is not stable in water solutions, leading to a Cl-OH substitution $YCu_3(OH)_{6+x}Cl_{3-x}$ with $x = 1/3$ [or $Y_3Cu_9(OH)_{19}Cl_8$] [10,11]. This substitution induces a distortion of the magnetic lattice as the Y atoms are moved out of the kagome plane [10]. The distorted kagome lattice of Cu^{2+} ions is scarcely studied with the exception of the family around $(Cs,Rb)_2Cu_3(Ti,Sn,Zr,Hf)F_{12}$ [12–15]. However, recent structural investigations of low-temperature diffraction on various kagome systems show that a structural instability induces distortions in barlowite, claringbullite [16], volborthite [17] and vesigneite [18] making it a typical structural motif at low temperatures.

In Y-kapellasite ($x = 1/3$) that we investigate in this paper, the distortion yields two nonequivalent Cu sites and a unique magnetic model with three different nearest-neighbor interactions, while still retaining rotational symmetry around the hexagons of the anisotropic kagome lattice (see inset Fig. 1 and Ref. [11]). The discovery of this compound has triggered a detailed theoretical study [19] which disclosed the full classical phase diagram of the model and its richness. Interestingly, besides two long-range ordered phases with propagation vectors $Q = (1/3, 1/3)$ and $Q = (0, 0)$, a large area in the phase diagram, coined "classical spin-liquid" phase, which encompasses the isotropic kagome model, opens up. It remains so far largely unexplored, although it could realize an unprecedented "jammed" spin-liquid phase, characterized by a discrete ground state degeneracy, in a disorder-free model. In addition, first-principle calculations confirm the relevance of this anisotropic nearest-neighbor model for Y-kapellasite and locates it in the $(1/3, 1/3)$ long-range ordered phase [19]. Here, we report a comprehensive study of the physical properties of large phase-pure single crystals that can be compared to the theoretical prediction and which show marked deviations

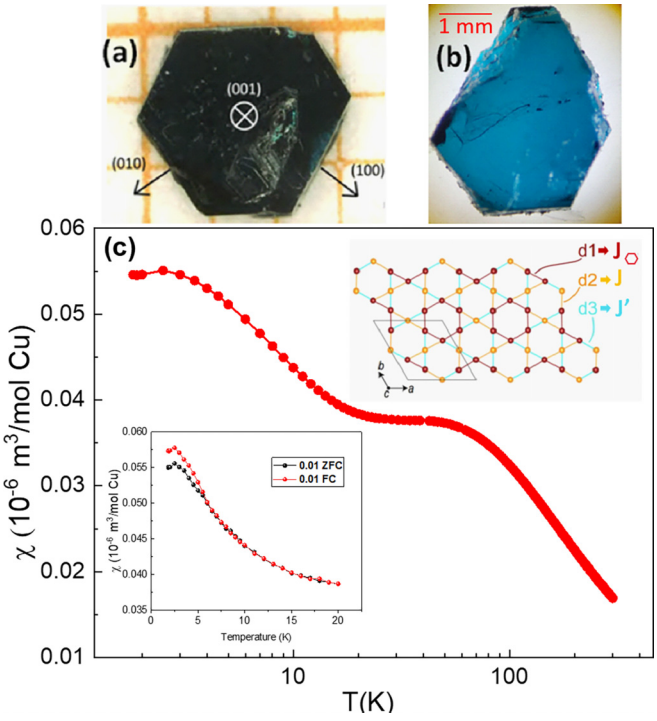

FIG. 1. (a) $Y_3Cu_9(OH)_{19}Cl_8$ single crystal along the c axis. (b) Image in transmission light of an as-grown single crystal. (c) Susceptibility (M/H) versus temperature with a 1 T field applied along c. Bottom-left inset: Field cooled (FC) and zero-field cooled (ZFC) measurements at 0.01 T. Upper-right inset: Anisotropic kagome lattice with three different nearest-neighbor Cu-Cu bonds and the related three different magnetic interactions.

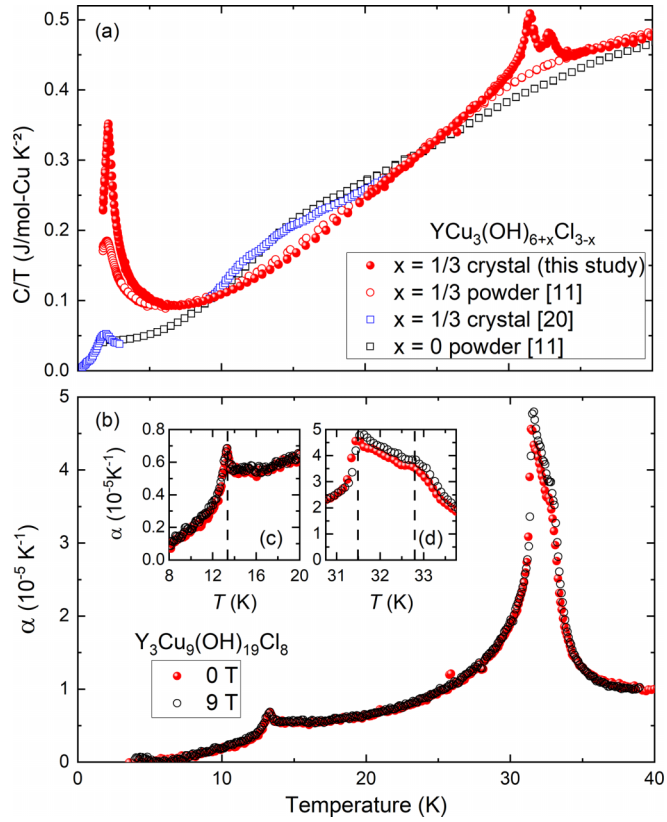

FIG. 2. (a) Specific heat divided by temperature in the temperature range from 1.8 to 40 K for the $x = 1/3$ optimized large crystals, compared to literature results for $x = 1/3$ and $x = 0$ powder samples [11] and the reported inclusion-free $x = 1/3$ crystals from Ref. [20]. (b) Thermal expansion along the c direction of an optimized large Y-kapellasite single crystal. (c) and (d) Insets: Enlarged views of the peaks detected in main panel (b). Note the different vertical scales in the two insets.

with respect to former studies of polycrystalline samples [11] or other synthesis routes for crystals [20].

The paper is organized as follows. In Secs. II and III the synthesis of phase-pure large single crystals is described and macroscopic measurements of the susceptibility, heat capacity, and thermal expansion are presented, providing evidence for a series of structural and magnetic transitions below 33 K. In Secs. IV and V, the transitions are investigated in detail by neutron diffraction and by Cl NMR, which show in particular good agreement with the theoretically predicted spin order in the ground state. In Sec. VI, muon-spin spectroscopy is used to prove the bulk nature of the 2.1-K magnetic transition. In Sec. VII, the spin-wave excitations are studied by inelastic neutron scattering and give an insight into the determination of the magnetic interactions beyond first-principle calculations. Finally in Sec. VIII, we summarize and discuss our results in comparison with previous ones on polycrystalline samples and in light of theoretical studies.

II. SYNTHESIS AND SUSCEPTIBILITY

The crystal growth of Y-kapellasite was originally reported in Ref. [10], where 0.59 g Y_2O_3, 0.82 g CuO, and 0.89 g $CuCl_2 \cdot 2(H_2O)$ in 10 ml H_2O were heated up to the dissolution point of Y_2O_3, followed by a slow cooling to crystallize. However, these crystals of an average size of $1 \times 1 \times 1$ mm^3 suffered small CuO inclusions since the growth takes place on the surface of the polycrystalline CuO starting material, as the dissolution point of Y_2O_3 and the crystallization point of the compound lie above the maximum in solubility of CuO. Reference [20] describes a synthesis of inclusion-free crystals using LiOH, $Y(NO_3)_3 \cdot 6H_2O$, and $CuCl_2 \cdot 2H_2O$. However, the reported crystals are somewhat disordered as a partial occupation of the Y site is observed, similarly to what was found in the related compound $YCu_3(OH)_6Cl_3$ [8]. This likely hints at a phase mixture in both cases due to contact with water. Indeed, a low percentage of occupation of Y for $YCu_3(OH)_6Cl_3$ [8] lies out of the kagome plane, which represents structural parts of Y-kapellasite $Y_3Cu_9(OH)_{19}Cl_8$. For the reported inclusion-free $Y_3Cu_9(OH)_{19}Cl_8$ [20], the partial occupation of Y can be explained similarly, since the specific heat shows a mixture of the signal observed for $x = 0$ and $x = 1/3$ as shown in Fig. 2.

We thus improved the synthesis for inclusion-free large bulk single crystals suitable for neutron studies via a horizontal external gradient growth method in a thick-walled quartz ampoule as described in detail for herbertsmithite in Ref. [21]. The growth is realized by slowly dissolving CuO in a YCl_3-H_2O (or YCl_3-D_2O for deuterated crystals) solution and transporting it to the cold end. The growth is executed in a three-zone furnace with a gradient of 25 °C and a temperature

of 240 °C at the hot end (note that the elevated pressure at this temperature requires especially thick quartz ampoules). The gradient was optimized as too low temperatures yielded a mixture of Y-kapellasite and clinoatacamite. Afterwards, the inclusion-free hexagonal single crystals have an average size of $3 \times 3 \times 1$ mm^3 up to $3 \times 3 \times 3$ mm^3, if grown over several weeks. The pictures of single-crystalline Y-kapellasite are displayed in Figs. 1(a) and 1(b), which show a transparent specimen without any visible impurity inclusions.

The dc susceptibility of a 15.7 mg single crystal of Y-kapellasite measured in a Quantum Design MPMS XL7 SQUID system with a 1 T field applied along the c axis is shown in Fig. 1(c). It reproduces published results [10,22], with an antiferromagnetic Curie-Weiss constant $\theta_{CW} = 102(1)$ K and $g_c = 2.40(1)$. Measurements in a lower 0.01 T magnetic field, shown in the inset, reveal a bifurcation of the field cooled and zero-field cooled curves below ∼5 K, and a maximum around 2.5 K. These low field measurements point at a magnetic transition which is investigated in detail with neutron scattering and resonance techniques in the following sections. At variance with Ref. [20], we observe no magnetic transition at 11 K (see Supplemental Material Fig. S1 in [23]). Such a transition, reminiscent of the one observed at 12 K in the $x = 0$ counterpart, supports a phase mixture scenario for the crystal of Ref. [20].

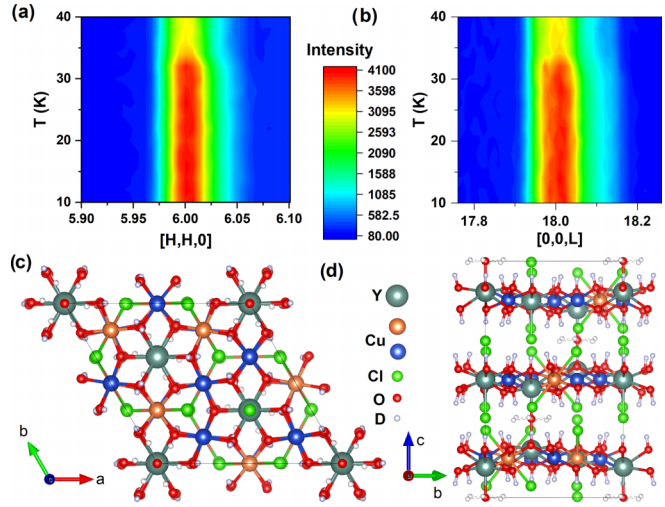

FIG. 3. Temperature scan, with a 2-K step, of the neutron diffraction intensity around the nuclear Bragg peaks (a) 660 and (b) 0018. The intensities in panel (b) have been multiplied by 4/3 to match those of panel (a). Structure obtained from neutron single crystal diffraction measurements at 40 K viewed along the (c) c axis and (d) a axis. Note the 1/6 partial occupancy of the six interlayer D1 positions.

III. SPECIFIC HEAT AND THERMAL EXPANSION

Specific heat was measured with the standard option of a Quantum Design Physical Properties Measurement System, using a 5.935-mg inclusion-free single crystal, formerly described. Its temperature evolution is shown in Fig. 2(a) and compared to the published results for $x = 0$ and $x = 1/3$ polycrystalline samples [11] and the $x = 1/3$ single crystal reported in Ref. [20]. Unexpectedly, our $x = 1/3$ single crystal presents a clear double peak at 33 K, which is absent in powder samples of the same compound. The underlying entropy amounts to 0.1537 J/mol K, below 3% of R ln2, calculated by using the powder sample as a baseline. There is no associated sharp feature in the susceptibility in this temperature range so that the double peak is likely signaling a structural transition. Note that this 33-K anomaly was not reported in the single crystals of Ref. [20] and that, on the contrary, the large hump around 15 K seen in the latter crystals and in the $x = 0$ powder sample, associated to magnetic transitions, is absent from our phase-pure $x = 1/3$ single crystal. Only at 2.1 K do we find a sharp peak in specific heat, which was already reported for this compound both in powder and crystals [10,11], and stems from a magnetic long-range ordering transition as shown later in this paper. For the disordered powder sample $x = 1/3$, the underlying entropy of the transition is reduced and previous muon-spin relaxation (μSR) studies had shown the absence of long-range order [11], possibly arising from the slightly altered structure due to the suppression of the 33-K transition.

To inspect the 33-K anomaly in more detail, we performed thermal expansion experiments along the crystallographic c axis, i.e., perpendicular to the kagome layers, using a capacitive dilatometer. Figure 2(b) displays the thermal expansion coefficient α on the same temperature scale as the specific heat data in panel (a). We find a similar anomaly below 33 K as in C/T, consisting of two slightly broadened, and thus overlapping peaks with a ratio between the sizes of the higher-temperature and lower-temperature peaks comparable to (a). The relative length change incorporated in these two sharp features amounts to $\Delta L/L = 10^{-4}$. In addition, we discover another, significantly smaller anomaly around 13 K, which can be seen in more detail in inset (c). Below 5 K an anomaly in α forms as approaching the transition at 2.1 K, signaling the importance of magnetoelastic coupling as antiferromagnetism sets in. Overall, the anomalies at 13 and 33 K reveal clear structural effects in this compound with a distorted kagome lattice, without noticeable changes upon applying a magnetic field of 9 T along the c axis.

IV. DIFFRACTION

The structure of Y-kapellasite $Y_3Cu_9(OH)_{19}Cl_8$ with R-3 was first reported in Ref. [10], where hydrogen was placed by symmetry arguments. Here one should note the unusual position of H1, which resides on six equivalent sites each with a 1/6 partial occupancy [see, e.g., Figs. 3(c) and 3(d). Later, from neutron diffraction on deuterated powder samples, we found that the deuterium atom next to the O1 refines to a distance above 1 Å, which is so far unaccounted for an O-H bound. Thus in Ref. [11], we dismissed the D1, leading to the revised chemical formula of $Y_3Cu_9(OD)_{18}OCl_8$. To further tackle this issue we then measured the stoichiometry including the hydrogen content with a combination of inductively coupled plasma mass spectroscopy (ICP-OES) and gas extraction, the former with a SPECTRO CIROS CCD and the latter with an Eltra ONH-2000 analyzer. For the determination of oxygen and hydrogen content, the powder samples were placed in a Ni crucible and clipped and heated, where the carrier gas takes the oxygen and hydrogen out

of the sample. The oxygen reacts with carbon, and CO_2 is detected in an infrared cell, while hydrogen is detected by a thermal conductivity cell. Each measurement was repeated three times and compared to a standard. The quoted error bars provide the statistical error. We thus measured three pieces of a hydrated single crystal and a part of a powder sample of Ref. [11]. The results of $Y_{3.00(3)}Cu_{9.06(9)}O_{19.0(2)}H_{18.7(3)}Cl_8$ for the crystals and $Y_{3.00(3)}Cu_{9.07(9)}O_{19.3(2)}H_{18.8(3)}Cl_8$ for the powder sample show a high enough hydrogen content to assume the ideal stoichiometry of $Y_3Cu_9(OH)_{19}Cl_8$. Notably we have also seen vibrational O-H modes that exist only for an electrical field parallel to the kagome plane solely matching to this hydrogen/deuterium position, further confirming the presence of the D1 atom. Therefore, from now on, we use the ideal stoichiometry of $Y_3Cu_9(OH)_{19}Cl_8$.

We performed neutron diffraction on the two-axis thermal neutron diffractometer D23 instrument at the Institut Laue-Langevin (ILL) using an inclusion-free, deuterated single crystal weighing 5.6 mg. Measurements have been performed in the temperature range of 40–0.065 K using constant incident neutron wavelength $\lambda = 1.27$ Å. The transition around 33 K observed in specific heat and thermal expansion is reflected here in an increase of the Bragg peak intensity [23]. Such an abrupt change of the intensity at the transition by about 30% is evident in the temperature scans of the 660 and 0018 Bragg peaks shown in Figs. 3(a) and 3(b). Yet, it produces no change in the crystallographic cell, as the crystallographic axes a, b, and c remain unaltered in the error bar range in the investigated temperature range.

We could reasonably refine all data with R-3 as well as a lowered symmetry (subgroup) R3, where in both cases, however, we find no clear change with temperature. The most plausible scenario is that the transition is arising from the D1, which remains mobile at higher temperatures and finally freezes at low temperatures leading to an effective lowering of symmetry to P1, where three different twin domains are realized. This scenario would realize a splitting of the Cl position as we observe in the following section. This symmetry change yields 174 atom positions with twin refinement that we could not carry out in the scope of this paper. We thus refined our data with the so far known R-3 structure where no major changes in the structure are observed. The Rietveld refinement results are summarized in Table I (see also [23]).

TABLE I. Rietveld refinement results of neutron diffraction data obtained at 65 mK, 8 K, 20 K, and 40 K with R-3 (No. 148) $a = b = 11.539$ Å, and $c = 17.1355$ Å.

T (K)	0.065			9			20			40		
	x/a	y/b	z/c	x/a	y/b	z/c	x/a	y/b	z/c	x/a	y/b	z/c
Y1	0	0	0.1318(7)	0	0	0.1314(6)	0	0	0.1324(7)	0	0	0.1302(5)
Y2	0	0	0.5	0	0	0.5	0	0	0.5	0	0	0.5
Cu1	0.6661(10)	0.8325(11)	0.5025(4)	0.6658(10)	0.8340(11)	0.5021(4)	0.6675(11)	0.8328(12)	0.5026(4)	0.6645(7)	0.8317(7)	0.5021(3)
Cu2	0.5	0	0.5	0.5	0	0.5	0.5	0	0.5	0.5	0	0.5
Cl1	0.6745(9)	0.0033(10)	0.2845(2)	0.6743(8)	0.0037(10)	0.28435(19)	0.6748(9)	0.0031(11)	0.2845(2)	0.6732(6)	0.0027(6)	0.28395(15)
Cl2	0	0	0.3368(5)	0	0	0.3368(5)	0	0	0.3365(6)	0	0	0.3373(4)
O1	0	0	0	0	0	0	0	0	0	0	0	0
D1	0.456(9)	0.776(10)	0.660(4)	0.455(9)	0.783(10)	0.664(4)	0.455(9)	0.776(10)	0.660(4)	0.462(7)	0.777(7)	0.661(3)
O2	0.8119(14)	0.8060(12)	0.5435(7)	0.8122(13)	0.8046(12)	0.5438(7)	0.8129(14)	0.8060(13)	0.5438(8)	0.8121(9)	0.8035(9)	0.5435(4)
D2	0.7769(19)	0.7778(17)	0.6011(9)	0.7874(18)	0.7858(17)	0.5991(9)	0.7723(17)	0.7722(16)	0.6030(8)	0.7866(13)	0.7827(13)	0.6005(6)
O3	0.5293(12)	0.6635(11)	0.5540(6)	0.5285(11)	0.6638(10)	0.5537(6)	0.5283(12)	0.6622(11)	0.5542(6)	0.5290(8)	0.6634(8)	0.5543(4)
D3	0.5494(17)	0.6731(18)	0.6065(8)	0.5575(16)	0.6709(17)	0.6082(8)	0.5452(15)	0.6740(18)	0.6051(8)	0.5548(12)	0.6692(13)	0.6069(5)
O4	0.5142(12)	0.8433(11)	0.4631(5)	0.5167(11)	0.8430(10)	0.4632(5)	0.5154(12)	0.8450(11)	0.4634(6)	0.5162(8)	0.8441(8)	0.4638(4)
D4	0.5008(16)	0.8310(17)	0.4096(8)	0.5013(16)	0.8328(16)	0.4097(8)	0.5018(17)	0.8320(17)	0.4099(8)	0.5029(12)	0.8337(12)	0.4099(6)

V. NUCLEAR MAGNETIC RESONANCE

We further investigated the structural distortions and magnetic transition using ^{35}Cl NMR on a ∼30-mg single crystal of Y-kapellasite $Y_3Cu_9(OH)_{19}Cl_8$ with an external magnetic field B_{ext} applied parallel to the c axis, i.e., perpendicular to the large facet of the sample (see Fig. 1). The spectra are measured from room temperature down to 5 K by sweeping the frequency in a fixed field $B_{ext} = 7.553$ T which corresponds to the reference frequency $\nu_0 = 31.510$ MHz. At lower temperatures, the broader spectra were recorded by sweeping the field with a fixed irradiation frequency ν_0.

The spectrum measured at 100 K, far above the magnetic transition and the structural distortions, is shown in Fig. 4. We observe two distinct central lines (see inset of Fig. 4) corresponding to the two crystallographic Cl sites with inten-

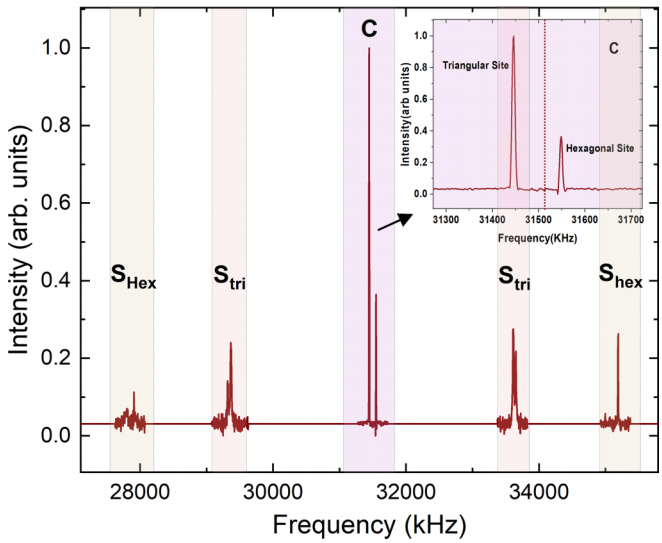

FIG. 4. Full NMR spectrum of ^{35}Cl at 100 K with the configuration $B_{\text{ext}} \parallel c$ which shows two central lines (C) of Cl1 (triangular site) and Cl2 (hexagonal site) and the two corresponding pairs of satellites (S_{tri} and S_{Hex}). Inset: Enhanced view of the central lines (C). The dashed vertical line indicates the reference frequency $\nu_0 =$ 31.510 MHz.

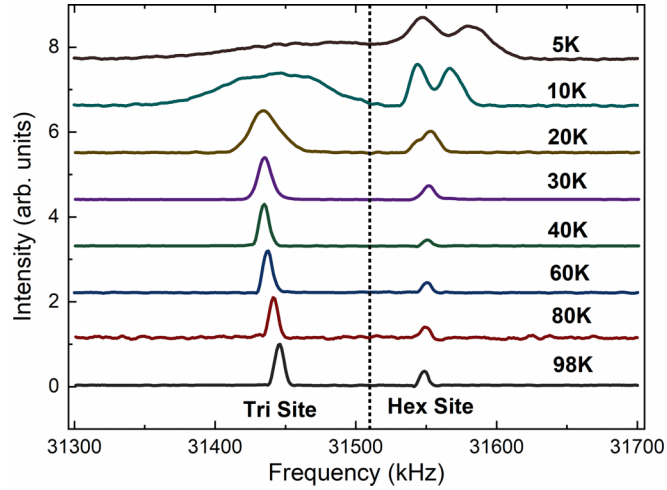

FIG. 5. Evolution of the central lines of the ^{35}Cl NMR spectra with temperature. The spectra are shifted vertically for clarity. Note the change of the width and the splitting of the hexagonal site line below 40 K which become prominent below 20 K. The dashed vertical line indicates the reference frequency.

sity ratio close to the expected 3:1. There are indeed 18 Cl1 (respectively, 6 Cl2) sites per unit cell located in between the kagome layers, close to the center of each triangle (respectively, hexagon) of the kagome structure. For clarity, in this section we denote the Cl1 and Cl2 sites as the triangular (*tri*) and hexagonal (*hex*) sites, respectively.

Since ^{35}Cl possesses a nuclear spin $I = 3/2$ with a finite quadrupolar moment, the three allowed transitions between the Zeeman-split adjacent nuclear levels are modified by the quadrupolar interaction with the surrounding electric charges. We therefore observe in the full spectrum three NMR lines per Cl site: One central line ($-1/2 \leftrightarrow 1/2$ transition) and two satellite ones ($-3/2 \leftrightarrow -1/2$ and $1/2 \leftrightarrow 3/2$ transitions).

At first order in perturbation, the frequency difference between two satellite lines of a given $\alpha = tri$ or $\alpha = hex$ Cl site arising from the quadrupolar interaction is given by [24]

$$\Delta\nu_\alpha^{(1)} = \nu_Q^\alpha(3\cos^2\theta_\alpha - 1 - \eta_\alpha \sin^2\theta_\alpha \cos 2\phi_\alpha), \qquad (1)$$

where θ_α and ϕ_α are the polar and azimuthal angles defining B_{ext} in the local frame of the principal axes of the electric field gradient (EFG) tensor, ν_Q^α is proportional to the quadrupolar moment and the largest eigenvalue of the EFG, therefore reflecting the strength of the quadrupolar interaction, and the asymmetry parameter η_α reflects the departure of the EFG from cylindrical symmetry.

Because of the high symmetry of the hexagonal Cl site, the EFG at this site is axially symmetric ($\eta_{\text{hex}} = 0$) along the c axis and, under the condition of the experiment $B_{\text{ext}} \parallel c$, $\theta_{\text{hex}} = 0$. For this site, the two satellites are maximally separated by $2\nu_Q^{\text{hex}}$ and we measure directly from Fig. 4 $\nu_Q^{\text{hex}} =$ 3640(5) kHz. The triangular Cl site is less symmetric. We used the structure determined at 40 K in Sec. IV by neutron diffraction to compute the EFG at this site with a point charge approach. From the calculated parameters $\theta_{\text{tri}} = 8.3°$, $\phi_{\text{tri}} =$ 123.0°, $\eta_{\text{tri}} = 0.33$ and the measured distance between satellites, we obtain with Eq. (1) the value $\nu_Q^{tri} = 2180(20)$ kHz. Note that if B_{ext} is not strictly applied along the symmetry axis c, the triangular sites become nonequivalent because of a different orientation of their EFG with respect to B_{ext}. The minute splitting of the triangular site satellite lines in Fig. 4 reflects such a small misalignment $\pm 1.2°$ of our crystal in the experiment.

The quadrupolar interaction shifts the position of the central line only at second order in perturbation [25]:

$$\nu_\alpha^{(2)} = -\frac{(\nu_Q^\alpha)^2}{2\nu_0} f(\theta_\alpha, \phi_\alpha, \eta_\alpha), \qquad (2)$$

where, for the simplest case of an axially symmetric EFG, f reads

$$f(\theta, \phi, 0) = \tfrac{3}{8}(1 - \cos^2\theta)(9\cos^2\theta - 1). \qquad (3)$$

In the present case at 100 K, the second-order quadrupolar shift is either $\nu_{\text{hex}}^{(2)} = 0$ since $\theta_{\text{hex}} = 0$ or negligible $\nu_{\text{tri}}^{(2)} = -4(1)$ kHz. The positions of the two central lines

$$\nu_\alpha^C = \nu_0\left(1 + K_\alpha^0 + K_\alpha^s\right) + \nu_\alpha^{(2)} \qquad (4)$$

are then rather set by the first term of magnetic origin, where K_α^0 is the temperature-independent orbital shift and K_α^s the spin shift arising from the polarization of the unpaired electron of the neighboring Cu^{2+} ions and therefore proportional to the spin susceptibility. From the plots of ν_α^C versus the susceptibility χ_c measured along the c direction in the range 100–300 K (not shown), we extract for the configuration $B_{\text{ext}} \parallel c$ the hyperfine constants $A_{\text{hex}} = 0.245(3)$ T/μ_B and $A_{\text{tri}} = -0.426(16)$ T/μ_B and the orbital terms $K_{\text{hex}}^0 = 120(10)$ ppm and $K_{\text{tri}}^0 = 52(10)$ ppm.

Figure 5 shows the evolution of the central lines upon cooling down to 5 K. Marked changes of the spectral shape are observed below 40 K where the structural distortions take place: The triangular site line broadens significantly and

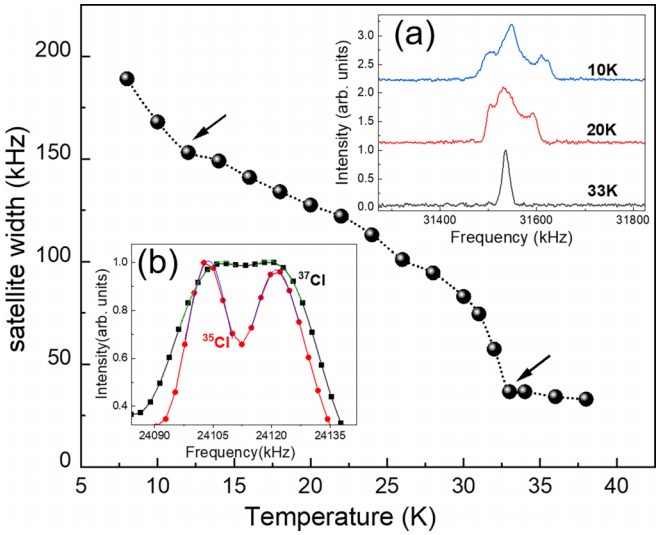

FIG. 6. Hexagonal satellite linewidth evolution with temperature which indicates two structural changes (black arrows). Inset (a) depicts the line shape changes occurring below 33 K for the hexagonal satellite. Inset (b) shows the hexagonal NMR central lines for ^{37}Cl and ^{35}Cl at 10 K.

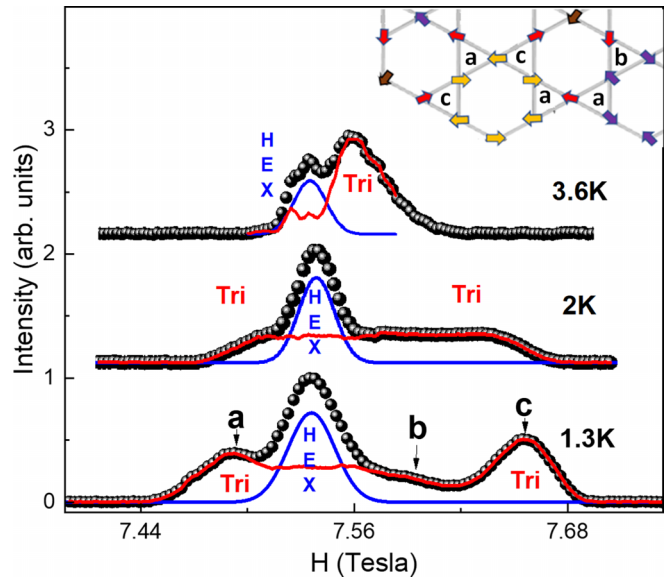

FIG. 7. Central line spectra at 1.3, 2, and 3.6 K and a partial view of the ground state spin texture proposed in Ref. [19] in the top-right corner. The spectra are shifted vertically for clarity. The blue line is a Gaussian fit of the hexagonal central line. This contribution is subtracted from the experimental spectrum to expose the triangular site one, shown as a red line. The triangle configurations **a**, **b**, and **c** yield three different dipolar fields at the triangular Cl site. Configurations **a** and **c** yield almost equal but opposite dipolar fields whereas configuration **b** has almost zero dipolar field along the z axis, i.e., the applied field direction.

the hexagonal one splits. Interestingly, although the changes appear in the range 30–40 K, they really get prominent only below 20 K where a second peak is observed in thermal expansion.

From the neutron diffraction study, the structural distortion at 33 K hardly changes the crystal structure and likely results from the freezing of the H1 proton on one of six equivalent positions. In the NMR spectra, the lowering of symmetry is clearly detected through the modification of the EFG. In particular, the splitting of the hexagonal site line implies the occurrence of at least two locally nonequivalent crystallographic sites, at variance with the R-3 structure, and at least one with a finite tilt $\theta_{\rm hex}$ of its EFG so that $\nu_{\rm hex}^{(2)}$ does not vanish in Eq. (4). From the measured splitting and using Eq. (4), we estimate $\theta_{\rm hex} \sim 5^\circ$ at 20 K and $\theta_{\rm hex} \sim 10^\circ$ at 10 K.

These changes of the local electrostatic environment of Cl affect even more clearly, at first order, the satellite lines. As shown in inset (a) of Fig. 6, the hexagonal satellite acquires a complex structure below 33 K pointing at even more than two nonequivalent sites. In order to determine the onset of the structural transition, we have measured the width of this satellite versus temperature as plotted in Fig. 6. Besides the abrupt change at the 33 K structural transition evidenced in heat capacity and neutron diffraction experiments, a marked change of the slope is detected at 13(1) K suggesting a secondary transition as detected in thermal expansion and also clearly in NMR relaxation measurements as discussed further in this section.

The 13-K transition is not magnetic as demonstrated by susceptibility measurements and muon-spin relaxation in the next section. To confirm the structural origin of the observed splitting at this temperature, we have compared the ^{35}Cl and ^{37}Cl NMR spectra at 10 K at the same reference frequency of 24.000 MHz. We have fitted the split hexagonal site central lines with Gaussian functions and compared the frequency differences $\Delta\nu^i$ between the two peak maxima for the two isotopes i [inset (b) in Fig. 6]. The ratio $\Delta\nu^{35}/\Delta\nu^{37} = 1.5(2)$ compares well to the square of the ratio of the quadrupolar moments of the two isotopes 1.61 as expected from Eq. (4). At variance, in the case of a magnetic origin with static internal fields, we would have observed a scaling with the gyromagnetic ratios of the two isotopes, i.e., a ratio ~1.20.

At lower temperatures ($T < 4.2$ K), the NMR lines broaden significantly, likely as a result of the building up of magnetic correlations, in line with the FC/ZFC divergence observed in this T range in the susceptibility (see Fig. 1). This magnetic broadening blurs the quadrupolar splitting and down to 2.1 K, we observe only two broad central lines, overlapping partially, for the two different, triangular and hexagonal, chlorine sites (see Fig. 7). At lower temperatures an abrupt broadening for the triangular site and a more moderate for the hexagonal one occurs, which represents the spectral NMR signature of the magnetic transition detected in the bulk, T_1 or μSR measurements. Actually, two triangular site peaks develop on both sides of the hexagonal central line and move away from each other upon cooling down. To quantify these evolutions, we compare in Fig. 8 the change of the linewidth $W(T)$ with temperature for the two sites.

In a recent theoretical study [19], a (1/3, 1/3) long-range magnetic order has been proposed for this system with a coplanar spin configuration reproduced partially in Fig. 7. Remarkably, for this predicted spin configuration, the hyperfine field at the hexagonal sites is zero (hexagons with different colors spins) or nearly zero (hexagons with same color spins).

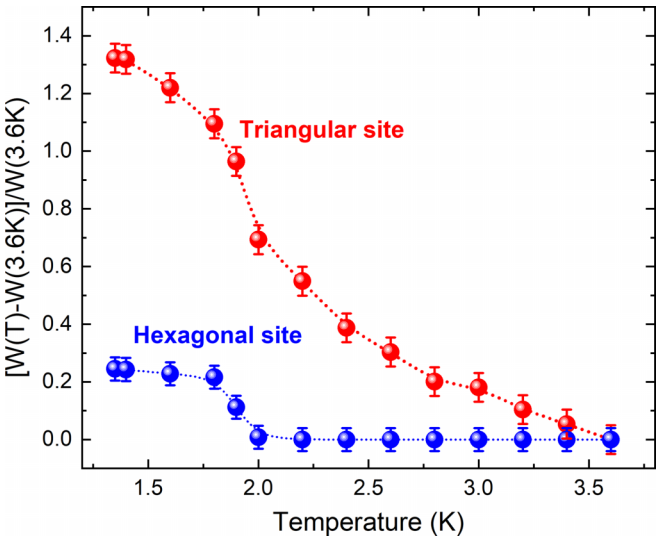

FIG. 8. Evolution versus temperature of the linewidth $W(T)$ for the triangular (red dots) and hexagonal (blue dots) sites.

At variance, for each triangle, two spins are nearly opposite leaving the third one uncompensated and thus able to yield a finite field at the triangular sites. There are actually three types of triangle configurations labeled **a**, **b**, and **c** in Fig. 7 corresponding to three different orientations of this uncompensated spin. For an anisotropic hyperfine tensor, we thus expect three different lines for the triangular Cl in the magnetically ordered phase. Although we could not determine experimentally all the components of the hyperfine tensor, we note that assuming a purely dipolar coupling, the shown spin configuration yield one very small and two almost equal but opposite z components of the transferred fields at the triangular Cl site. Thus, the low-temperature spectrum supports at least qualitatively the theoretically proposed order, both for the triangular and the hexagonal Cl sites.

Figure 9 shows the evolution with temperature of the spin-lattice relaxation rate (T_1^{-1}) measured using the saturation recovery sequence at both Cl sites. Being quadrupolar active, Cl nuclei probe both the magnetic and structural fluctuations. In the temperature evolution of T_1^{-1} the structural distortions at ∼33 and ∼13 K discussed earlier are clearly observed as a sharp and broad peak, respectively, together with the magnetic transition around ∼2.1 K.

To extract the T_1 values, the recovery curves of the nuclear magnetization $M(t)$ at each temperature were fitted to [26]

$$M(t) = M_{\text{sat}}\left(1 - ae^{-(t/T_1)^{\beta}} - be^{-(6t/T_1)^{\beta}}\right), \qquad (5)$$

where $a + b = 1$, $a = 0.1$ and 0.12, respectively, for the hexagonal and triangular sites, and $\beta \leqslant 1$ is a phenomenological stretching parameter used to account for a possible distribution of T_1 [27]. The evolution of $\beta(T)$ for both sites is shown as insets in Fig. 9. While a single value of T_1 is measured at high temperature ($\beta = 1$), an increasingly broader distribution ($\beta < 1$) is needed upon cooling down toward the structural and magnetic transitions, likely pointing at the building up of spatial correlations. During the transition regimes, we could fix the value of β with no noticeable reduction of the fit quality, to avoid artifacts in the determination of the peaks of the correlated T_1^{-1} quantity.

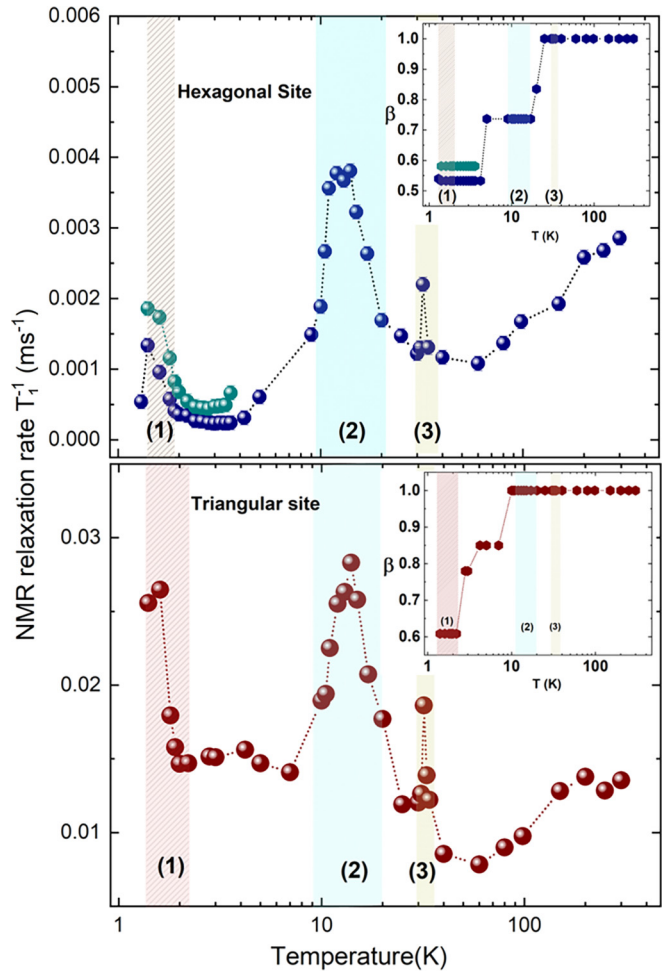

FIG. 9. Plots of ^{35}Cl NMR relaxation rate T_1^{-1} versus temperature measured at the hexagonal (top) and triangular (bottom) central line positions. The two structural transition regimes (2) and (3) and the magnetic one (1) are highlighted. The T_1 distribution parameter β is plotted in the inset. Below 5 K, when the NMR lines of the two sites overlap, T_1 was also measured at the isolated hexagonal satellite position (dark-cyan dots) and shows the same behavior as the central line.

VI. MUON-SPIN RELAXATION

To elucidate the nature of the ground state of Y- kapellasite, we performed a μSR experiment on the GPS and DOLLY instruments at the PSI muon facility from the paramagnetic regime (>20 K) down to 0.28 K. The 100% spin-polarized muons are implanted at time zero in the sample, where they stop at the most electronegative positions. The muon spins evolve in the local fields until the muons decay into positrons, emitted preferentially in the last direction of the muon spins after a mean lifetime of 2.2 μs. By collecting the positrons emitted forward and backward with respect to the muon beam direction, the muon decay asymmetry, proportional to muon-spin polarization can be recorded versus time and allows

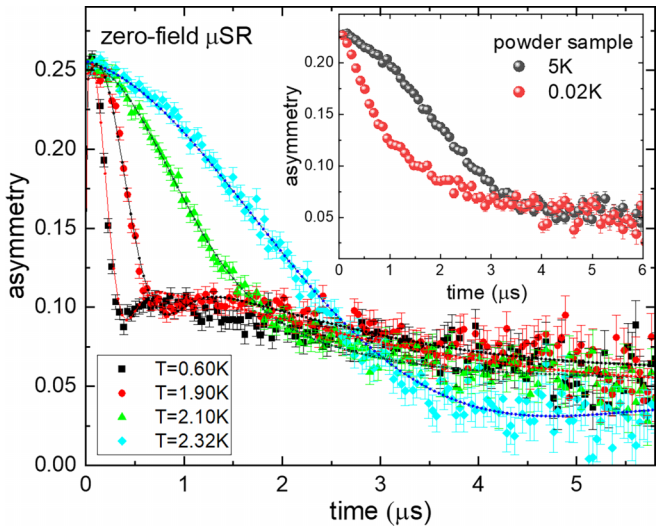

FIG. 10. Time evolution of the zero-field (ZF) muon decay asymmetry at some selected temperatures in single-crystal samples. Lines are fit to Eq. (9). Inset: Powder sample data from Ref. [11].

one to characterize the internal fields and their fluctuations [28–30].

For this μSR experiment, we used two coaligned phase-pure single crystals of sizes $\sim 3 \times 3 \times 1$ mm^3 with their c axis parallel to the initial muon-spin direction. The muon decay asymmetry in zero external field (ZF) is depicted at some selected temperatures in Fig. 10. At low temperature, the asymmetry evidently differs from previous measurements [11] on a powder sample shown in the inset, with a much faster relaxation and a characteristic damped oscillation signaling static internal fields.

Above 2.5 K, the relaxation hardly depends on temperature [23] nor on the nature of the sample, powder or single crystal. The electronic spins are fast fluctuating in their paramagnetic regime, and the relaxation is dominated by the quasistatic, weak and random, nuclear fields. Following the model used for the powder sample [11], we fitted the muon decay asymmetry at high temperature to

$$a_0 P_{\text{para}}(t) = a_0[f P_{\text{OH}}(t) + (1-f) K T_{\Delta_{\text{Cl}}}(t)], \qquad (6)$$

where

$$P_{\text{OH}}(t) = e^{-\left(\Delta_{\text{OH}}^2 t^2/2\right)}\left[\frac{1}{6} + \frac{1}{3}\cos\left(\frac{\omega_{\text{OH}} t}{2}\right) + \frac{1}{3}\cos\left(\frac{3\,\omega_{\text{OH}} t}{2}\right) + \frac{1}{6}\cos\left(\omega_{\text{OH}} t\right)\right]. \qquad (7)$$

The latter $P_{\text{OH}}(t)$ stands for the formation of μOH complexes with a pulsation $\omega_{\text{OH}} = \frac{\hbar \mu_0 \gamma_\mu \gamma_{\text{H}}}{4\pi d^3}$ which depends on the μ-H distance d, the gyromagnetic ratios $\gamma_{\text{H}} = 267.513$ Mrad/s/T and $\gamma_\mu = 851.616$ Mrad/s/T, respectively, for protons and muons, and a Gaussian broadening Δ_{OH} due to the other surrounding nuclear spins. The second term in Eq. (6) is a static Kubo-Toyabe relaxation standing for the minority fraction $1-f$ of muon stopping sites, likely close to the Cl^- ions, where they experience a Gaussian distribution of static nuclear fields with a width Δ_{Cl}. The parameter $a_0 = 0.255$ is the initial muon decay asymmetry in our experimental conditions.

TABLE II. Static nuclear parameters derived from high-temperature fit of the ZF asymmetry with Eq. (6).

Static parameters	$Y_3Cu_9(OH)_{19}Cl_8$
f%	75.00 ± 1.00
ω_{OH} (Mrad s^{-1})	0.55 ± 0.02
d (Å)	1.63 ± 0.02
Δ_{Cl} (μs^{-1})	0.09 ± 0.02
Δ_{OH} (μs^{-1})	0.208 ± 0.02

The nuclear relaxation parameters in Eqs. (6) and (7) evaluated by fitting the ZF muon polarization at 20 K are presented in Table II.

Upon cooling, the relaxation from the electronic spins increases progressively and below 2.1 K, at variance with the powder sample [11], a strongly damped oscillation develops, conclusively indicating a magnetic transition in the single-crystal samples (Fig. 10). Below 1.5 K, the asymmetry could be fitted accordingly to

$$a_0 P_f(t) = a_0\left[\frac{2}{3}\cos(\omega_f t + \phi) e^{-\sigma^2 t^2/2} + \frac{e^{-\lambda_f t}}{3}\right] \qquad (8)$$

which accounts for a magnetically frozen single phase with an average internal field at the muon sites $B_{\text{int}} = \omega_f/\gamma_\mu$. The damping parameter σ encodes the width of the distribution of these internal fields. The last exponential term accounts for residual fluctuations in the frozen phase. At base temperature $T = 0.28$ K, we obtain $B_{\text{int}} = 8.6$ mT which is almost twice lower than the lowest internal fields previously reported in the closely related $x = 0$ variant of $YCu_3(OH)_6O_xCl_{3-x}$ [11,31] and more than ten times lower than in barlowite [5] with similar Cu-OH bonds. In the latter, the 101(2) mT static field at the μOH site arises from an average 0.38 μ_B copper moment. By comparison, we roughly estimate that the Cu^{2+} moment in Y-kapellasite is strongly reduced down to about $1/30\,\mu_B$.

In order to fit the asymmetry on the whole temperature range, we combined both Eqs. (6) and (8) in

$$a_0 P(t) = a_0\left[f_f P_f(t) + (1-f_f) P_{\text{para}}(t) e^{-\lambda_p t}\right] \qquad (9)$$

with a switching parameter f_f that tracks the frozen volume fraction from fully ordered for $f_f = 1$ to fully paramagnetic for $f_f = 0$. All the nuclear parameters are kept constant, so that the only varying parameters shown in Fig. 11 are the frozen fraction, the oscillation frequency and its damping rate, and the relaxation rate λ_p or λ_f for the paramagnetic or the frozen phase. The latter show a clear peak at 2.1 K as expected for the critical slowing down of the fluctuations at the magnetic transition. Surprisingly, there is a singular point at 1.56 K in the relaxation rate plot but no significant changes in other variable parameters at the same temperature. Although this feature demands further confirmation, it is reminiscent of the spin dynamics reentrance reported in clinoatacamite [32] and echoes an anomaly reported in the low-temperature magnetization measurements [22].

To conclude, from our μSR measurements, Y-kapellasite shows a completely frozen ground state in the case of single crystals in contrast to the fluctuating ground state observed in the powder sample. The relaxation rate variation with temper-

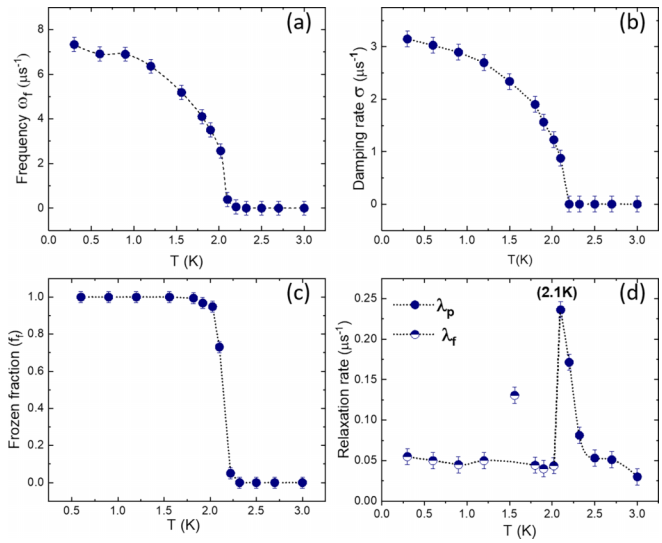

FIG. 11. Temperature evolution of the parameters used in Eq. (9) to fit the ZF μSR data: (a) frequency ω_f reflecting the internal field magnitude, (b) damping rate σ, (c) fraction f_f of the frozen phase, and (d) relaxation rates in the paramagnetic (λ_p) and frozen (λ_f) phases.

ature indicates a phase transition at ∼2.1 K where the internal static fields set in. At 0.28 K, deep in the magnetic phase state, we estimate a strongly reduced frozen moment for the Cu^{2+} of about $1/30\,\mu_B$.

VII. TIME-OF-FLIGHT NEUTRON SCATTERING

With large deuterated single crystals of $Y_3Cu_9(OD)_{19}Cl_8$ at hand, we also performed inelastic neutron scattering on this anisotropic kagome antiferromagnet in order to probe the magnetic excitations in reciprocal space and to identify the magnetic order [33]. Inelastic neutron scattering (INS) measurements were performed on the IN5 disk chopper time-of-flight spectrometer [34] at the Institut Laue-Langevin on a collection of single crystals with a total mass of 0.3 g. These crystals were coaligned in the (H, H, L) horizontal plane and glued on a thin aluminum plate with the hydrogen-free CYTOP solution (CTL-809M). Measurement runs were performed at a constant temperature with an incident neutron wavelength $\lambda = 4.8$ Å (incident energy $E_i = 3.55$ meV, giving a FWHM energy resolution of 0.08 meV) or $\lambda = 2.6$ Å ($E_i = 12.1$ meV), while the sample stage was rotated around the direction perpendicular to the beam, to map out the reciprocal space. The detectors efficiency was corrected by a preliminary measurement on a vanadium can.

Magnetic scattering could be identified only below 3 meV, an unexpected feature given the large antiferromagnetic Curie-Weiss temperature of $\theta_{CW} = -100$ K [10]. We thus focused on measurements using our low incident energy of 3.55 meV and followed the temperature evolution of the dynamical neutron structure factor $S(q, E)$. Figure 12 shows the intensity contour color plots of $S(q, E)$ along the $[H, H, 0]$ direction. At 60 K there is a large phonon contribution that substantially reduces at 20 K and below, where nearly ver-

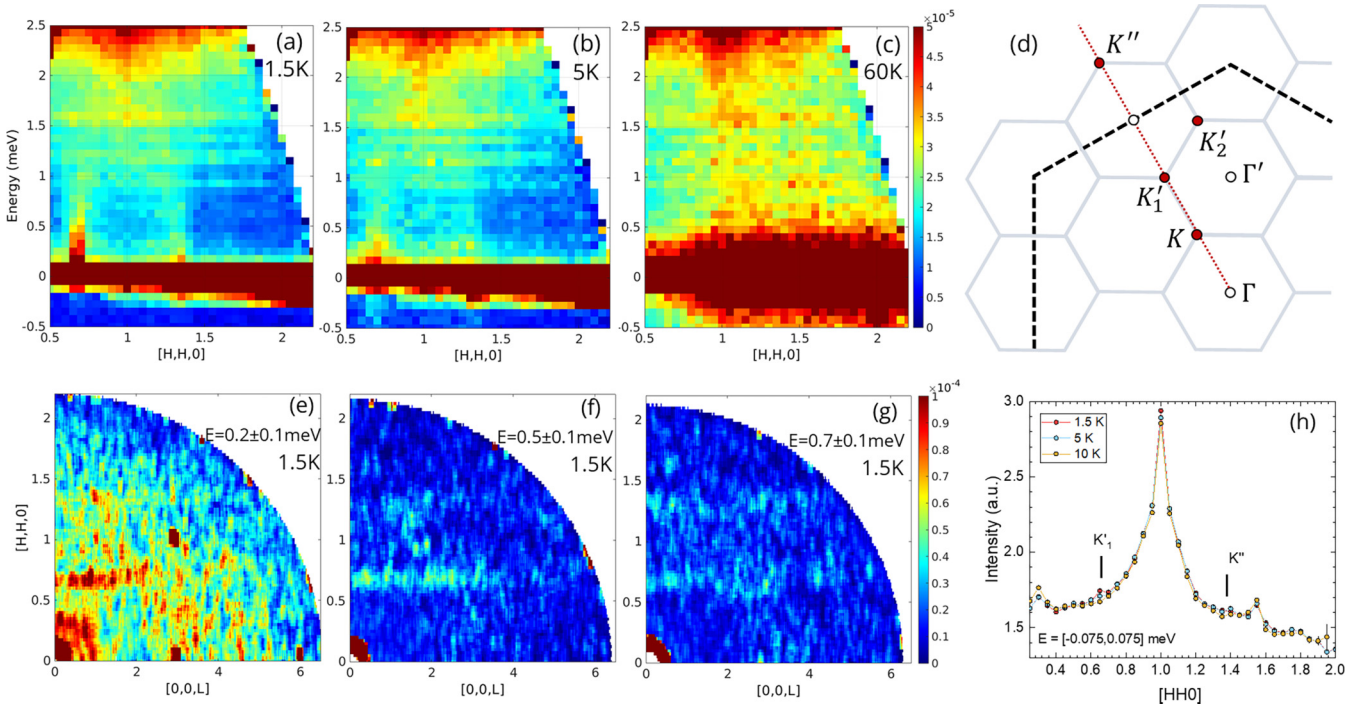

FIG. 12. (a)–(c) Evolution in temperature of the dynamical structure factor $S(q, E)$ along the $[H, H, 0]$ direction (integrated over $L = [-6, 6]$) at $T = 1.55$ K, $T = 5$ K, and $T = 60$ K. (d) Brillouin zone boundaries (gray lines) with K and Γ points and extended Brillouin zone (black dashed line) in the reciprocal space. The red dotted line represents the $[H, H, 0]$ direction. (e)–(g) Evolution in energy of $S(q, E)$ in the (H, H, L) plane at $T = 1.55$ K. (h) INS measurement integrated in energy over the elastic resolution and in the range $-6 < L < 6$, showing a weak increase at 1.5 K at the K_1' position and possibly also at K'', characteristic of the $(1/3, 1/3)$ magnetic order. The other discernible peaks are not of magnetic origin.

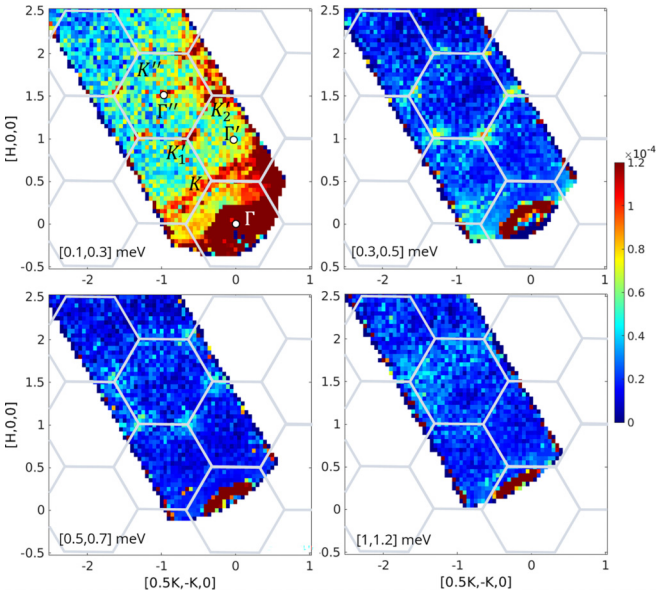

FIG. 13. Dynamical structure factor $S(Q, E)$ for the $(H, K, 0)$ plane measured at $T = 1.55$ K. The four color plot maps show its evolution in energy with the corresponding integrated energy range. Gray lines indicate the Brillouin zone boundaries. Bright spots of intensity are observed at the K points, and correspond to the dispersion of spin waves.

tical columns of intensity become apparent close to $K_1' = (2/3, 2/3, 0)$ and $K'' = (4/3, 4/3, 0)$, with a region of broad intensity located around 2 meV and close to [1,1,0]. At our base temperature of 1.5 K, sharp dispersive features emerge from these two Q positions which we identify as spin-wave excitations. They show a pronounced two-dimensional character, as revealed by the presence of rods of scattering intensity along the $[0, 0, L]$ direction [Figs. 12(e)–12(g)], and thus justify the two-dimensional Heisenberg kagome antiferromagnet model applied below. From this time-of-flight measurement, one can isolate the elastic contribution by integrating over twice the energy resolution (∼0.15 meV) only. Figure 12(h) shows such contribution with the apparition of tiny q-resolution limited magnetic Bragg peaks at 1.5 K located at the K_1' position and less clearly at the K'' one. This elastic scattering points to a small ordered fraction of the Cu^{2+} moment, that could be easily missed in a conventional energy-integrated neutron diffraction experiment, and strongly supports a magnetic noncollinear coplanar phase with a $Q = (1/3, 1/3)$ ordering wave vector.

The inelastic scattering in the $(H, K, 0)$ plane is displayed in Fig. 13. The energy-integrated cuts show clear intensities located at the K positions of the Brillouin zone, mirroring the sharp spin-wave dispersions already observed below 1 meV in Fig. 12(a). Above 1 meV, the inelastic scattering broadens significantly and extends toward the Brillouin zone center.

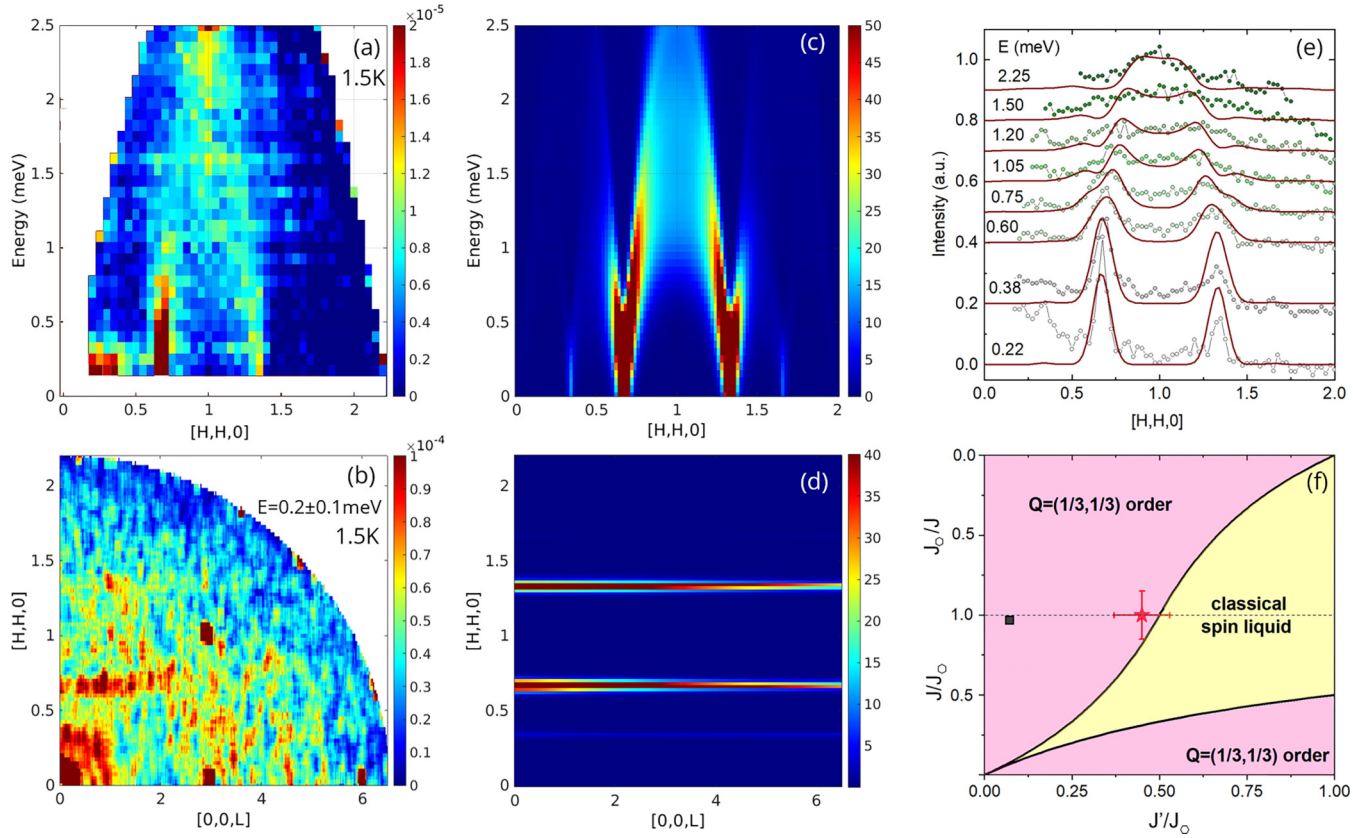

FIG. 14. Comparison between experimental data (a), (b) and spin-wave simulations (c), (d) at $T = 1.5$ K. The INS data in (a) measured at 1.5 K was subtracted by a 5-K dataset (see text) to highlight the magnetic contribution. (e) Energy-integrated cuts along $[H, H, 0]$ of data shown in (a) and (c) for different energies E with an integration range of 0.15 meV. Symbols are for data and lines for the simulation. They are both shifted vertically for clarity. (f) Classical phase diagram reproduced from [19]. The black square denotes the position found from DFT calculation [19] while the red star locates Y-kapellasite using the exchange couplings found in our work.

To better isolate the inelastic magnetic contribution present at 1.5 K, we subtracted a background constructed by the replication of the 5 K dataset, integrated in the range $H = [1.6, 2]$, along $[H, H, 0]$, where the phonon and magnetic contributions appear to be minimal. The result is shown in Fig. 14(a). The dispersive excitations rising from K_1' and K'' are clearly singled out, and then merge into a broad arch extending from 1 to 2.5 meV. Guided by the observation of an in-plane distortion of the kagome lattice, and by the recent *ab initio* density functional theory (DFT) results [19], we performed linear spin-wave calculations using the SPINW package [35] of the Heisenberg model with only nearest-neighbor interactions in order to model the excitations on such an anisotropic kagome lattice:

$$\mathcal{H} = \sum_{\langle i,j \rangle} J_{ij} \boldsymbol{S_i} \cdot \boldsymbol{S_j}, \tag{10}$$

where J_{ij} can take three different values $J_{\hexagon}$, J, and J' depending, respectively, on the bonds d_1, d_2, and d_3 as defined in Fig. 1. From DFT calculation, Hering *et al.* [19] confirmed the relevance of such spin models in the context of Y-kapellasite using three antiferromagnetic couplings $J \simeq J_{\hexagon} \simeq 140$ K and $J' \simeq 10$ K. The spin-wave simulations assumed an enlarged unit cell of nine sites, because of the two different copper sublattices, and a coplanar order with a $Q = (1/3, 1/3)$ propagation vector, as described in detail in Ref. [19]. The $J = J_{\hexagon} = J'$ case leads to the well-known $\sqrt{3} \times \sqrt{3}$ phase of the classical kagome antiferromagnetic model which fails to reproduce our data when $J > 15$ K, due to the maximum of the band observed around 2.5 meV. Given that $\theta_{CW} = -100$ K imposes a higher exchange value, we discard the isotropic case and instead study the excitations for the parameters $J = J_{\hexagon}$ and $J' \neq J$. From the evolution of the spin-wave spectrum with J or J', we find our best model using $J \simeq J_{\hexagon} = 140$ K and $J' = 63$ K. However, we also find that a single set of interactions cannot account for the spread of intensity observed at [1,1,0], from 1 to 2.5 meV. Instead, we consider a ∼10% distribution of J', tentatively attributed to some local disorder, and that could indeed satisfactorily fit our inelastic data, as shown in Figs. 14(c)–14(e), leading to $J \simeq J_{\hexagon} = 140(10)$ K and $J' = [56, 70]$ K. Finally, we note that the intensity observed at low Q, near $Q = (1/3, 1/3, 0)$, and below 0.5 meV [see Fig. 14(a)] is much broader than predicted by the simulation, and may hint at a more complex ground state in Y-kapellasite with the presence of short-range order and fluctuations. We note that this broad intensity extends mostly around the zone boundaries of the first Brillouin zone (Fig. 13) and not close to the boundaries of the *extended* Brillouin zone, as predicted for the classical spin liquid [19].

In summary, INS gives evidence for elastic scattering below 5 K, in agreement with the static magnetism revealed by μSR and line broadening in NMR, consistent with a $Q = (1/3, 1/3)$ magnetic ground state. Furthermore, we found a set of magnetic interactions in Y-kapellasite which is in very good agreement with the predictions from DFT and variational Monte Carlo studies [19]. The main difference is our experimental value of $J' \simeq 63(7)$ K as compared to the theoretical estimate $J' = 10.3(7)$ K. This locates Y-kapellasite in the $Q = (1/3, 1/3)$ magnetic order of the phase diagram, but very close to the classical spin-liquid phase reported in Ref. [19].

VIII. DISCUSSION AND CONCLUSION

Our experimental investigation of $Y_3Cu_9(OH)_{19}Cl_8$ reveals an unusual bidimensional coplanar $Q = (1/3, 1/3)$ long-range ordered ground state, overall in very good agreement with the theoretical study in Ref. [19]. In particular, the proposed spin arrangement in the ground state is found to be compatible with the Cl NMR line shape at low temperature. However, at variance with first-principle calculations where the third interaction of the model J' was found to be negligible, we determine experimentally a finite $J' \lesssim J_{\hexagon}/2$. This finding of a sizable antiferromagnetic J' seems nonetheless consistent with the Cu-OH-Cu bond angles which vary only by 4.6° among the three different bonds. The smallest angle 113.1° corresponding to J' remains significantly larger than 105° which is known to yield small ∼− 15 K ferromagnetic interaction in Zn-kapellasite [36].

In addition, to reproduce the broad magnetic excitations in INS, a distribution ∼10% of the J' interaction was imposed. This suggests some kind of disorder. Due to the large difference in the ionic radii of Y^{3+} and Cu^{2+} we expect no significant intersite mixing at variance with Zn-kapellasite or other Zn- and Cu-based kagome materials and indeed we found no evidence of such disorder in the magnetic lattice above 33 K, neither in neutron diffraction nor in NMR which on the contrary exposes well-resolved narrow lines. Therefore, the distribution of J' may arise only at low temperature, as a result of the structural instabilities observed at 33 and 13 K. The slightly different local environment detected below 33 K by Cl NMR would then reflect in the moderate distribution of the interaction, while preserving on average the high-temperature magnetic model, since the lattice parameters and the magnetic lattice remain unchanged within our accuracy in diffraction experiments on the whole temperature range, down to 65 mK.

The experimentally determined interactions locate Y-kapellasite in the classical phase diagram close to the boundary between the $(1/3, 1/3)$ long-range ordered and the classical spin liquid phases [see Fig. 14(f)]. Although the effect of quantum fluctuations has not been investigated so close to the phase boundary, we may anticipate that they are responsible for the strongly reduced value of the Cu^{2+} moments $\lesssim 0.1\,\mu_B$, which could not be detected in standard neutron diffraction but yield static internal fields detected both in NMR and μSR. The proximity to a phase boundary may also help in understanding the striking difference in the ground states of the present large single-crystal samples and formerly studied polycrystalline ones [11]. Indeed in the latter, the moments were found to remain fluctuating in the ground state and also no structural transition was detected. We may assume that some additional disorder in the polycrystalline samples or slightly different interactions, due to the absence of structural transition, destabilize the fragile ordered state observed in large single crystals. We note that such a sensitivity to the sample crystallinity seems to be a common feature of anisotropic kagome compounds

such as volborthite [17,37] or vesigneite [18,38,39]. The fragility of the ground state in all these compounds seems to originate from a subtle interplay between structure and magnetic frustration.

Beyond the proposed anisotropic nearest-neighbor model, and despite its apparent success to reproduce the physics in $Y_3Cu_9(OH)_{19}Cl_8$, one important perspective to complete our understanding of this material is to quantify and address the role of Dzyaloshinskii-Moriya interaction. Let us indeed recall that this anisotropy of the interaction was pointed out as the main ingredient driving long-range order in the sister compound $YCu_3(OH)_6Cl_3$ [40] with a perfect kagome lattice. Quantum fluctuations and especially their role at the phase boundaries and how they impact the jammed classical spin-liquid phase is another key perspective of this work. Finally we note that a Br counterpart [41] was recently synthesized, showing no sign of ordering, and likely allowing to span further the phase diagram of the anisotropic kagome model.

ACKNOWLEDGMENTS

The authors acknowledge the support of the French Agence Nationale de la Recherche, under Grant No. ANR-18-CE30-0022 "LINK", the financial support of the Fondation Charles Defforey-Institut de France and funding from Deutsche Forschungsgemeinschaft (DFG) through TRR 288-422213477 (project A03). We thank Samir Hammoud for carrying out the ICP and gas extraction experiments, V. Baldent for his help on the interpretation of neutron diffraction results, and A. Razpopov, R. Valenti, H.O. Jeschke and J. Reuther for useful discussions and for sharing INS simulation data.

[1] L. Balents, Spin liquids in frustrated magnets, Nature (London) **464**, 199 (2010).

[2] J. R. Chamorro, T. M. McQueen, and T. T. Tran, Chemistry of quantum spin liquids, Chem. Rev. **121**, 2898 (2021).

[3] P. Mendels, F. Bert, M. A. de Vries, A. Olariu, A. Harrison, F. Duc, J. C. Trombe, J. S. Lord, A. Amato, and C. Baines, Quantum Magnetism in the Paratacamite Family: Towards an Ideal Kagomé Lattice, Phys. Rev. Lett. **98**, 077204 (2007).

[4] T.-H. Han, J. S. Helton, S. Chu, D. G. Nocera, J. A. Rodriguez-Rivera, C. Broholm, and Y. S. Lee, Fractionalized excitations in the spin-liquid state of a kagome-lattice antiferromagnet, Nature (London) **492**, 406 (2012).

[5] K. Tustain, B. Ward-O'Brien, F. Bert, T. Han, H. Luetkens, T. Lancaster, B. M. Huddart, P. J. Baker, and L. Clark, From magnetic order to quantum disorder in the Zn-barlowite series of $S = 1/2$ kagomé antiferromagnets, npj Quantum Mater. **5**, 74 (2020).

[6] Y. Fu, M.-L. Lin, L. Wang, Q. Liu, L. Huang, W. Jiang, Z. Hao, C. Liu, H. Zhang, X. Shi, J. Zhang, J. Dai, D. Yu, F. Ye, P. A. Lee, P.-H. Tan, and J.-W. Mei, Dynamic fingerprint of fractionalized excitations in single-crystalline $Cu_3Zn(OH)_6FBr$, Nat. Commun. **12**, 1 (2021).

[7] P. Puphal, K. M. Zoch, J. Désor, M. Bolte, and C. Krellner, Kagome quantum spin systems in the atacamite family, Phys. Rev. Mater. **2**, 063402 (2018).

[8] W. Sun, Y.-X. Huang, S. Nokhrin, Y. Pan, and J.-X. Mi, Perfect Kagomé lattices in $YCu_3(OH)_6Cl_3$: A new candidate for the quantum spin liquid state, J. Mater. Chem. C **4**, 8772 (2016).

[9] Y. Fu, L. Huang, X. Zhou, J. Chen, X. Zhang, P. Chen, S. Wang, C. Liu, D. Yu, H.-F. Li, L. Wang, and J.-W. Mei, $LnCu_3(OH)_6Cl_3$ (Ln = Gd, Tb, Dy): Heavy lanthanides on spin-1/2 kagome magnets, Chin. Phys. B **30**, 100601 (2021).

[10] P. Puphal, M. Bolte, D. Sheptyakov, A. Pustogow, K. Kliemt, M. Dressel, M. Baenitz, and C. Krellner, Strong magnetic frustration in $Y_3Cu_9(OH)_{19}Cl_8$: A distorted kagome antiferromagnet, J. Mater. Chem. C **5**, 2629 (2017).

[11] Q. Barthélemy, P. Puphal, K. M. Zoch, C. Krellner, H. Luetkens, C. Baines, D. Sheptyakov, E. Kermarrec, P. Mendels, and F. Bert, Local study of the insulating quantum kagome antiferromagnets $YCu_3(OH)_6O_xCl_{3-x}(x = 0, 1/3)$, Phys. Rev. Mater. **3**, 074401 (2019).

[12] M. Müller and B. G. Müller, $Cs_2Cu_3MIVF_{12}$ (MIV = Zr, Hf) – Kristallstruktur und magnetische Eigenschaften, Z. Anorg. Allg. Chem. **621**, 993 (1995).

[13] K. Matan, T. Ono, G. Gitgeatpong, K. de Roos, P. Miao, S. Torii, T. Kamiyama, A. Miyata, A. Matsuo, K. Kindo, S. Takeyama, Y. Nambu, P. Piyawongwatthana, T. J. Sato, and H. Tanaka, Magnetic structure and high-field magnetization of the distorted kagome lattice antiferromagnet $Cs_2Cu_3SnF_{12}$, Phys. Rev. B **99**, 224404 (2019).

[14] L. Downie, E. Ardashnikova, C. Tang, A. Vasiliev, P. Berdonosov, V. Dolgikh, M. de Vries, and P. Lightfoot, Novel $S = 1/2$ kagome lattice materials: $Cs_2TiCu_3F_{12}$ and $Rb_2TiCu_3F_{12}$, Crystals **5**, 226 (2015).

[15] M. S. Grbić, S. Krämer, C. Berthier, F. Trousselet, O. Cépas, H. Tanaka, and M. Horvatić, Microscopic Properties of the Pinwheel Kagome Compound $Rb_2Cu_3SnF_{12}$, Phys. Rev. Lett. **110**, 247203 (2013).

[16] A. Henderson, L. Dong, S. Biswas, H. I. Revell, Y. Xin, R. Valenti, J. A. Schlueter, and T. Siegrist, Order–disorder transition in the $S = \frac{1}{2}$ kagome antiferromagnets claringbullite and barlowite, Chem. Commun. **55**, 11587 (2019).

[17] H. Ishikawa, M. Yoshida, K. Nawa, M. Jeong, S. Krämer, M. Horvatić, C. Berthier, M. Takigawa, M. Akaki, A. Miyake, M. Tokunaga, K. Kindo, J. Yamaura, Y. Okamoto, and Z. Hiroi, One-Third Magnetization Plateau with a Preceding Novel Phase in Volborthite, Phys. Rev. Lett. **114**, 227202 (2015).

[18] D. Boldrin, K. Knight, and A. S. Wills, Orbital frustration in the $S = 1/2$ kagome magnet vesignieite, $BaCu_3V_2O_8(OD)_2$, J. Mater. Chem. C **4**, 10315 (2016).

[19] M. Hering, F. Ferrari, A. Razpopov, I. I. Mazin, R. Valentí, H. O. Jeschke, and J. Reuther, Phase diagram of a distorted kagome antiferromagnet and application to Y-kapellasite, npj Comput. Mater. **8**, 10 (2022).

[20] W. Sun, T. Arh, M. Gomilšek, P. Koželj, S. Vrtnik, M. Herak, J.-X. Mi, and A. Zorko, Magnetic ordering of the distorted kagome antiferromagnet $Y_3Cu_9(OH)_{18}[Cl_8$ (OH)] prepared via optimal synthesis, Phys. Rev. Mater. **5**, 064401 (2021).

[21] T. H. Han, J. S. Helton, S. Chu, A. Prodi, D. K. Singh, C. Mazzoli, P. Müller, D. G. Nocera, and Y. S. Lee, Synthesis and characterization of single crystals of the spin-$\frac{1}{2}$ kagome-lattice antiferromagnets $Zn_xCu_{4-x}(OH)_6Cl_2$, Phys. Rev. B **83**, 100402(R) (2011).

[22] T. Biesner, S. Roh, A. Razpopov, J. Willwater, S. Süllow, Y. Li, K. M. Zoch, M. Medarde, J. Nuss, D. Gorbunov, Y. Skourski, A. Pustogow, S. E. Brown, C. Krellner, R. Valentí, P. Puphal, and M. Dressel, Multi-center magnon excitations open the entire Brillouin zone to terahertz magnetometry of quantum magnets, Adv. Quantum Technol. **5**, 2200023 (2022).

[23] See Supplemental Material at http://link.aps.org/supplemental/10.1103/PhysRevB.107.125156 for the crystallographic information files corresponding to the refined Y-kapellasite $Y_3Cu_9(OH)_{19}Cl_8$ structure at 40, 20, 8, and 0.065 K and additional susceptibility, diffraction, and μSR data.

[24] M. Cohen and F. Reif, Quadrupole effects in nuclear magnetic resonance studies of solids, *Solid State Physics* (Elsevier, New York, 1957), Vol. 5, pp. 321–438.

[25] J. F. Baugher, P. C. Taylor, T. Oja, and P. J. Bray, Nuclear magnetic resonance powder patterns in the presence of completely asymmetric quadrupole and chemical shift effects: Application to metavanadates, J. Chem. Phys. **50**, 4914 (1969).

[26] A. Suter, M. Mali, J. Roos, and D. Brinkmann, Mixed magnetic and quadrupolar relaxation in the presence of a dominant static Zeeman Hamiltonian, J. Phys.: Condens. Matter **10**, 5977 (1998).

[27] H. Choi, I. Vinograd, C. Chaffey, and N. Curro, Inverse Laplace transformation analysis of stretched exponential relaxation, J. Magn. Reson. **331**, 107050 (2021).

[28] F. Bert, Local probes of magnetism, NMR and μSR: A short introduction, Collection SFN **13**, 03001 (2014).

[29] S. Blundell, Spin-polarized muons in condensed matter physics, Contemp. Phys. **40**, 175 (1999).

[30] A. D. Hillier, S. J. Blundell, I. McKenzie, I. Umegaki, L. Shu, J. A. Wright, T. Prokscha, F. Bert, K. Shimomura, A. Berlie *et al.*, Muon spin spectroscopy, Nat. Rev. Meth. Primers **2**, 4 (2022).

[31] A. Zorko, M. Pregelj, M. Klanjšek, M. Gomilšek, Z. Jagličić, J. S. Lord, J. A. T. Verezhak, T. Shang, W. Sun, and J.-X. Mi, Coexistence of magnetic order and persistent spin dynamics in a quantum kagome antiferromagnet with no intersite mixing, Phys. Rev. B **99**, 214441 (2019).

[32] X. G. Zheng, H. Kubozono, K. Nishiyama, W. Higemoto, T. Kawae, A. Koda, and C. N. Xu, Coexistence of Long-Range Order and Spin Fluctuation in Geometrically Frustrated Clinoatacamite $Cu_2Cl(OH)_3$, Phys. Rev. Lett. **95**, 057201 (2005).

[33] E. Kermarrec, P. Puphal, J. Willwater, Q. Barthélemy, S. Süllow, and J. Ollivier, Spin excitation spectra in the kagome candidate material $Y_3Cu_9(OH)_{19}Cl_8$, Institut Laue-Langevin (ILL) (unpublished).

[34] J. Ollivier and H. Mutka, IN5 cold neutron time-of-flight spectrometer, prepared to tackle single crystal spectroscopy, J. Phys. Soc. Jpn. **80**, SB003 (2011).

[35] S. Toth and B. Lake, Linear spin wave theory for single-Q incommensurate magnetic structures, J. Phys.: Condens. Matter **27**, 166002 (2015).

[36] B. Fåk, E. Kermarrec, L. Messio, B. Bernu, C. Lhuillier, F. Bert, P. Mendels, B. Koteswararao, F. Bouquet, J. Ollivier, A. D. Hillier, A. Amato, R. H. Colman, and A. S. Wills, Kapellasite: A Kagome Quantum Spin Liquid with Competing Interactions, Phys. Rev. Lett. **109**, 037208 (2012).

[37] F. Bert, D. Bono, P. Mendels, F. Ladieu, F. Duc, J.-C. Trombe, and P. Millet, Ground State of the Kagomé-Like $S = 1/2$ Antiferromagnet Volborthite $Cu_3V_2O_7(OH)_2 \cdot 2H_2O$, Phys. Rev. Lett. **95**, 087203 (2005).

[38] J. A. Quilliam, F. Bert, R. H. Colman, D. Boldrin, A. S. Wills, and P. Mendels, Ground state and intrinsic susceptibility of the kagome antiferromagnet vesignieite as seen by ^{51}V NMR, Phys. Rev. B **84**, 180401(R) (2011).

[39] M. Yoshida, Y. Okamoto, M. Takigawa, and Z. Hiroi, Magnetic order in the spin-1/2 kagome antiferromagnet vesignieite, J. Phys. Soc. Jpn. **82**, 013702 (2013).

[40] T. Arh, M. Gomilšek, P. Prelovšek, M. Pregelj, M. Klanjšek, A. Ozarowski, S. J. Clark, T. Lancaster, W. Sun, J.-X. Mi, and A. Zorko, Origin of Magnetic Ordering in a Structurally Perfect Quantum Kagome Antiferromagnet, Phys. Rev. Lett. **125**, 027203 (2020).

[41] Z. Zeng, X. Ma, S. Wu, H.-F. Li, Z. Tao, X. Lu, X.-h. Chen, J.-X. Mi, S.-J. Song, G.-H. Cao, G. Che, K. Li, G. Li, H. Luo, Z. Y. Meng, and S. Li, Possible Dirac quantum spin liquid in the kagome quantum antiferromagnet $YCu_3(OH)_6Br_2[Br_x(OH)_{1-x}]$, Phys. Rev. B **105**, L121109 (2022).